Materials Theory

ORIGINAL ARTICLE Open Access

Modeling mesoscale fission gas behavior in UO_2 by directly coupling the phase field method to spatially resolved cluster dynamics

Dong-Uk Kim[1], Sophie Blondel[2], David E. Bernholdt[3], Philip Roth[3], Fande Kong[4], David Andersson[5], Michael R. Tonks[1*] and Brian D. Wirth[2,3]

*Correspondence: michael.tonks@ufl.edu
[1] University of Florida, Gainesville, FL, USA
Full list of author information is available at the end of the article

This manuscript has been partially authored by UT-Battelle, LLC, under contract DE-AC05-00OR22725 with the US Department of Energy (DOE) and by Battelle Energy Alliance, LLC under Contract No. DE-AC07-05ID14517 with DOE. The US government retains and the publisher, by accepting the article for publication, acknowledges that the US government retains a nonexclusive, paid-up, irrevocable, worldwide license to publish or reproduce the published form of this manuscript, or allow others to do so, for US government purposes. DOE will provide public access to these results of federally sponsored research in accordance with the DOE Public Access Plan (http://energy.gov/downloads/doe-public-access-plan).

Abstract

Fission gas release within uranium dioxide nuclear fuel occurs as gas atoms diffuse through grains and arrive at grain boundary (GB) bubbles; these GB bubbles grow and interconnect with grain edge bubbles; and grain edge tunnels grow and connect to free surfaces. In this study, a hybrid multi-scale/multi-physics simulation approach is presented to investigate these mechanisms of fission gas release at the mesoscale. In this approach, fission gas production, diffusion, clustering to form intragranular bubbles, and re-solution within grains are included using spatially resolved cluster dynamics in the Xolotl code. GB migration and intergranular bubble growth and coalescence are included using the phase field method in the MARMOT code. This hybrid model couples Xolotl to MARMOT using the MultiApp and Transfer systems in the MOOSE framework, with Xolotl passing the arrival rate of gas atoms at GBs and intergranular bubble surfaces to MARMOT and MARMOT passing evolved GBs and bubble surface positions to Xolotl. The coupled approach performs well on the two-dimensional simulations performed in this work, producing similar results to the standard phase field model when Xolotl does not include fission gas clustering or re-solution. The hybrid model performs well computationally, with a negligible cost of coupling Xolotl and MARMOT and good parallel scalability. The hybrid model predicts that intragranular fission gas clustering and bubble formation results in up to 70% of the fission gas being trapped within grains, causing the increase in the intergranular bubble fraction to slow by a factor of six. Re-solution has a small impact on the fission gas behavior at 1800 K but it has a much larger impact at 1000 K, resulting in a twenty-times increase in the concentration of single gas atoms within grains. Due to the low diffusion rate, this increase in mobile gas atoms only results in a small acceleration in the growth of the intergranular bubble fraction. Finally, the hybrid model accounts for migrating GBs sweeping up gas atoms. This results in faster intergranular bubble growth with smaller initial grain sizes, since the additional GB migration results in more immobile gas clusters reaching GBs.

Keywords: Phase-field method, Cluster dynamics, Multi-scale simulation, MOOSE framework

Introduction

Fission gas behavior in uranium dioxide (UO_2) nuclear fuels is a key factor in determining fuel performance, because the diffusion and precipitation of xenon (Xe) and krypton (Kr) in fission gas bubbles influences both the fuel swelling and the quantity of fission gas released to the fuel rod plenum (Olander, 1976; Rest et al., 2019; Tonks et al., 2018a). Fission gas bubbles within the fuel significantly contribute to swelling (White et al., 2006), decrease fuel thermal conductivity (Tonks et al., 2016), increase crack probability by increasing internal stresses and weakening the material (OGUMA, 1982; Chakraborty et al., 2016; Jiang et al., 2020), impact other microstructure evolution such as grain growth (Ainscough et al., 1973; Tonks et al., 2021), and determine the rate of fission gas release (Lösönen, 2000). Once fission gas is released from the fuel, it lowers the gap conductivity and raises the cladding pressure (Olander, 1976; Rest et al., 2019; Tonks et al., 2018a).

Fission gas behavior leading to release may be categorized in three stages (which all occur simultaneously) according to the location of the dominating physics (Tonks et al., 2018a). The first stage is intragranular fission gas behavior, including the generation, diffusion, clustering and bubble formation, and re-solution of fission gas atoms in the fuel matrix. In this stage, fission gas clustering with vacancies results in the creation of intragranular bubbles. The second stage is the intergranular fission gas behavior on grain boundaries (GBs) or grain faces. Fission gas bubbles nucleate on GBs and then grow and interconnect. As a percolated network of bubbles form, more and more of the grain face bubbles come in contact with GB triple junctions or grain edges. The third stage is the fission gas behavior along the grain edges. Bubbles on the grain edges quickly connect to form networks of grain edge tunnels that eventually contact free surfaces, allowing fission gas to escape the fuel and enter the open volume within the fuel rod.

Most fission gas behavior models used for fuel performance calculations trace back to the 1957 formulation by Booth (Booth, 1957), the late 1960's formulation by Speight and co-workers (Speight, 1969; Cornell et al., 1969), or the more recent work by Turnbull (Turnbull et al., 1982), White and Tucker (White & Tucker, 1983), and Forsberg and Massih (Forsberg & Massih, 1985; Massih & Forsberg, 2008). These models typically rely on a small number of spatially-independent partial differential equations (PDEs), or even a single PDE, to model transport of gas atoms to GBs that occurs in stage one. They also include the concept of an effective diffusivity to account for the effect of intragranular fission gas bubbles on the bulk diffusion rate (Massih & Forsberg, 2008). More recently, additional physically-based fission gas bubble models have been developed by Pastore and co-workers (Pastore et al., 2013; Pastore et al., 2018; Pizzocri et al., 2018), based on a simplified cluster dynamics framework. In these reduced models, the bubble interconnection in stage two is modeled as a simple percolation threshold for the gas that has reached GBs. Gas that exceeds the threshold is instantly released, neglecting stage three by assuming that the transport of fission gas to free surfaces through grain edge tunnels is instantaneous.

These models are over-simplifications of the actual behavior of noble gas within the fuel. The treatment of intragranular bubbles in these models is very simplified, with the characteristics of the bubble population (number density, mean size) given as constant parameters or calculated through simplistic, empirically-based functions of temperature

(White & Tucker, 1983; Forsberg & Massih, 1985; Pastore et al., 2013). However, the actual intragranular bubble evolution is complex and strongly depends on the specific fuel irradiation conditions and reactor operating history (Lösönen, 2000; Kashibe et al., 1993; Baker, 1977). In addition, the simple percolation threshold used in these models completely neglects the complexities of intergranular bubble interconnection observed in experiments and the critical role of grain edge tunnels (White, 2004). These simplifications were made due to the complexity of actual fission gas behavior and to reduce the computational cost of legacy fuel performance codes so they could run on the computers of that time. These gaps in current fission gas release and swelling models limit their accuracy and their applicability to altered conditions, such as higher burnup or doped UO_2. Therefore, improving the representation of fission gas bubble evolution, both intra- and intergranular, is a key issue in achieving higher standards of accuracy in fuel performance analysis.

One approach that has been taken to improve the physical description of intragranular fission gas behavior is to incorporate mean-field cluster dynamics approaches (Pastore et al., 2018; Pizzocri et al., 2018), in which gas atom and vacancy cluster complexes evolve over time, including the transfer of gas atoms and vacancies between clusters. Mean-field cluster dynamics has been applied to model bubble behavior in Kr-implanted and annealed UO_2 (Skorek et al., 2012). It has also been used with atomic-scale simulation results to investigate Xe diffusion in UO_2 (Matthews et al., 2019; Matthews et al., 2020) and doped UO_2 (Cooper et al., 2020). In addition to mean-field cluster dynamics, which does not consider the spatial location of the clusters, cluster dynamics can also resolve a spatial domain in multiple dimensions (Dunn et al., 2013; Dunn & Capolungo, 2015; Dunn et al., 2016). Such methods have been applied to simulate radiation defects and gas behavior in solids for fusion plasma facing components (Xu & Wirth, 2010; Wirth et al., 2015; Maroudas et al., 2016; Blondel et al., 2018). The strength of the cluster dynamics method is that it directly models the nucleation and growth of noble gas bubbles, and naturally incorporates very small clusters (bubble nuclei) that are continually forming and dissolving. The limitations of cluster dynamics are associated with the computational expense of modeling large bubbles. For example, if we assume a xenon density of $10^{28}\,\mathrm{m}^{-3}$ within a fission gas bubble, then a 10 nm radius bubble would contain in excess of 40,000 xenon atoms and would require at least 40,000 degrees of freedom (DoFs) to model.

The phase field method is another computational approach that has been used to model fission gas bubble behavior (Millett & Tonks, 2011; Li et al., 2017; Tonks et al., 2018b). In phase field models of fission gas (Aagesen et al., 2019; Hu et al., 2009; Millett et al., 2011; Millett et al., 2012), conserved thermodynamic variable fields are used to represent defects, including fission gas atoms and vacancies. Non-conserved variable fields are used to represent bubbles and grains, having a value of one in their corresponding grain or bubble and a value of zero elsewhere. These variable fields smoothly transition between values, such that bubble surfaces and GBs have a diffuse interface with a finite width. They are evolved over time to minimize the free energy of the system. Source terms are used to add defects due to fission and radiation damage. The strength of phase field models of fission gas behavior is that they can efficiently model evolving bubbles and can naturally represent the co-evolution of bubbles and GBs over time.

Thus, they are well suited to investigate the interconnection of grain face and edge bubbles (Aagesen et al., 2019; Millett et al., 2012; Aagesen et al., 2020). Limitations include that they cannot naturally model nucleation and that they cannot efficiently model small bubbles within much larger simulation domains because large systems of equations are generated. For example, a polycrystal simulation with a 10 μm average grain size could efficiently model GB bubbles with radii around 50 nm, but they could not feasibly include one to two nm radius intragranular bubbles.

There have been efforts by Hu and collaborators to represent small defects within large simulation domains of uranium molybdenum (UMo) by representing the small defects with spatially-varying fields similar to what is done in spatially-resolved cluster dynamics (Hu et al., 2016; Hu et al., 2017; Hu et al., 2020). They first investigated fission gas release in UMo using a modified Booth approach (Hu et al., 2016) in which variable fields were used to evolve the intragranular bubble population trapping gas migrating towards grain boundaries. They then used a similar treatment of intragranular bubbles along with fields representing vacancy, interstitial, and interstitial loop densities and coupled them with a phase field model of recrystallization in UMo (Hu et al., 2017). Finally, they coupled a spatially-resolved cluster dynamics model of vacancy and interstitial clusters with a phase field model of fission gas bubble evolution, including nucleation of gas bubbles informed by the cluster concentrations (Hu et al., 2020).

In this work, we present a hybrid model in which a spatially-resolved cluster dynamics model is directly coupled to a phase field fission gas model, such that the growth and interconnection of intergranular bubbles can be modeled, while also resolving the nucleation, growth, and re-solution of intragranular gas bubbles. Our hybrid model is similar to the model from Hu et al. (Hu et al., 2020) in that a spatially-resolved cluster dynamics model is coupled to a phase field model of fission gas behavior; however, in our model the cluster dynamics is focused on the transport and clustering of gas within UO_2 grains and the phase field is focused on intergranular gas behavior and GB migration. Thus, the combined model can represent all three stages of fission gas release in UO_2 and provide a powerful means of investigating fission gas behavior. We begin by summarizing the hybrid model and ensuring the accuracy of the coupling in Section 2. Then, in Section 3, we assess its parallel performance. Finally, in Section 4, we investigate the predicted bubble behavior, including the impact of clustering and re-solution, the impact of temperature, and the impact of the grain size.

The hybrid cluster dynamics/phase field model

In this section, we summarize the approach and capabilities of our new hybrid model. We start by summarizing the cluster dynamics code, Xolotl, and the phase field code, MARMOT, as well as the specific models implemented in each code. We then discuss the method used to couple the codes. We end with a model comparison that was used to ensure that the coupling between the codes is functioning correctly.

Xolotl cluster dynamics code

The intragranular fission gas behavior is modeled by Xolotl, a cluster dynamic code originally developed to simulate irradiated material in fusion reactors (Xu & Wirth, 2010; Wirth et al., 2015; Maroudas et al., 2016; Blondel et al., 2018; Blondel et al.,

2017). To simplify the model, it assumes that all fission gas atoms are Xe, the most common component of the noble gas atoms produced by fission. In addition, in this work the UO_2 vacancies are not explicitly modeled and only Xe atoms and Xe clusters/bubbles are modeled. Vacancies and interstitials will be added in future work. Xolotl evolves the concentrations of clusters containing increasing numbers of Xe atoms. The evolution of each cluster size is determined by solving a PDE generally described as:

$$\frac{\partial C_n}{\partial t} = \dot{F} y_n + D_n \nabla^2 C_n - Q(C_n), \tag{1}$$

where C_n is the concentration of a cluster containing n Xe atoms, the first right-hand-side term corresponds to the production of new Xe, the second term is the diffusion term, and the third term accounts for reactions between clusters. The xenon production is a function of the fission rate density $\dot{F}$ and the fission yield y_n of n Xe atoms per fission; fissions only yield single Xe atoms, such that $y_{n>1}=0$. The diffusion rate for a given cluster is defined by its diffusion coefficient D_n. The single Xe atom is the sole cluster considered mobile in the current model, such that $D_{n>1}=0$ and D_1 is defined by the functional form for the diffusion coefficient from Turnbull (Turnbull et al., 1982). Three types of reactions are allowed: self-clustering to form larger Xe bubbles $Xe_1 + Xe_n \rightarrow Xe_{n+1}$, and single Xe atom emission and single Xe atom re-solution, both defined by $Xe_n \rightarrow Xe_1 + Xe_{n-1}$. The general form of the reaction term for clusters of size $n \geq 2$ is:

$$Q(C_n) = k_n C_n C_1 - k_{(n-1)} C_{(n-1)} C_1 + k_n^{emit} C_n - k_{(n+1)}^{emit} C_{(n+1)} + k_n^{reso} C_n - k_{(n+1)}^{reso} C_{(n+1)}, \tag{2}$$

with reaction rates:

$$k_n = 4\pi D_1 (r_1 + r_n),$$

$$k_{(n+1)}^{emit} = (k_n/\Omega) \times \exp(-E_b/(k_B \times T)), \tag{3}$$

where D_1 is the single Xe diffusion coefficient, r_n is the reaction radius for a bubble made of n Xe atoms, Ω is the atomic volume, E_b is the binding energy of Xe_{n+1}, k_B is the Boltzmann constant, and T is the temperature. The reaction radius for a single Xe atom is set to 0.3 nm and a Xe density of $10.16\,\mathrm{nm}^{-3}$ is used to describe the bubble size based on the number of Xe atoms in a cluster/bubble. The binding energy of Xe_2 is set to 1.85 eV and the energies increase linearly to reach a constant value of 7 eV for $n > 30$, based on estimates obtained from atomistic molecular dynamics simulations performed by Liu and Andersson (Liu & Andersson, 2015). Re-solution of single Xe atoms into the bulk from intragranular bubbles is included using the heterogeneous re-solution model from Setyawan et al. (Setyawan et al., 2018). The re-solution reaction rate is expressed as:

$$k_n^{reso} = \left(a_1 \exp\left(-b_1\, r_n\right) + \frac{\left(y(0) - a_1\right)}{1 + c\ r_n^2} \exp\left(-b_2 r_n^2\right) \right) 1.0 \times 10^4\, \dot{F}, \tag{4}$$

where a_1, b_1, $y(0)$, b_2, and c are taken from Table III of Setyawan et al. (Setyawan et al., 2018) for the recommended value of $\zeta = 0.73$. The reaction term for a single xenon atom sums the contribution from each reaction:

$$Q(C_1) = \sum\nolimits_{n \geq 2} \left[k_n C_n C_1 - k_{(n+1)}^{emit} C_{(n+1)} \right] + 2k_1 C_1^2 - 2k_2^{emit} C_2 - 2k_2^{reso} C_2. \tag{5}$$

The PDEs are solved using the finite difference method (FDM) and implicit time integration with PETSc (Blondel et al., 2018). Xolotl uses a uniform grid to model the spatial domain with periodic boundary conditions. The grid points corresponding to GBs and bubble surfaces are treated like free surfaces, meaning that the concentration vectors at these grid points are forced to 0.0 when the solution is updated in the solver at each time step. At each grid point Xolotl can compute the current single Xe concentration and the volume fraction $\sum_{n > n_{min}} C_n \times V_n$, with the cluster volume calculated as a sphere whose radius is the reaction radius and n_{min} an optional minimum size. On each grid point located at an interface, Xolotl also computes the total Xe rate from single Xe atoms diffusing from nearby grid points and from any Xe clusters at the interface location resulting from migration of the interface.

MARMOT phase field model

The phase field method is a common numerical approach used to predict spatially-resolved microstructure evolution. In the phase field method, microstructural features are represented by the values of continuous variable fields. The fields smoothly transition between values at interfaces, such as GBs or bubble surfaces, giving the interfaces a finite width. The phase field method has been used to simulate and investigate various physical phenomena (Chen, 2002; Moelans et al., 2008; Tonks & Aagesen, 2019), including radiation damage and nuclear materials (Millett & Tonks, 2011; Li et al., 2017; Tonks et al., 2018b). It has been applied to model fission gas bubbles in UO_2 by various researchers, with various assumptions and approximations depending on the phenomena of interest (Aagesen et al., 2019; Millett et al., 2012; Li et al., 2013; Zhu & Hallberg, 2015). In this work, we use the model from Aagesen et al. (Aagesen et al., 2019) that was developed to investigate the evolution of intergranular gas bubbles in polycrystalline UO_2. While we refer the reader to Ref. (Aagesen et al., 2019) for a complete description of the model, we summarize it, below.

In this model, the material microstructure is represented by various continuous variable fields. Non-conserved order parameters are used to distinguish voids (ϕ_0) and the various UO_2 grains (ϕ_i, $i = 1, \ldots N$, where N is the number of grains), where the order parameters are equal to one in their corresponding region and zero in the other regions. The interfaces between these regions (bubble surfaces for transitions from void to grains and GBs for transitions from one grain to another) have a finite width of l. The model explicitly represents fission gas atoms (treated as Xe atoms) and uranium lattice vacancies (the

oxygen lattice is neglected, as the uranium lattice is rate limiting), where both have distinct equilibrium concentrations in the UO_2 grains and in the voids. As mentioned in the previous section, uranium vacancies are not considered in the cluster dynamics model in Xolotl. We have chosen to include vacancies in the phase field model because we plan to use our hybrid model in the future to investigate behaviors in which vacancies and gas atoms act independently. It will facilitate that investigation if the phase field model already includes vacancies and Xe atoms. Rather than directly solving for the concentrations of gas atoms and vacancies, we solve for their chemical potentials μ_g and μ_v. The concentrations c_g *and* c_v can then be determined from the chemical potentials. The order parameters and chemical potentials are evolved with time to minimize the free energy of the system according to the equations:

$$\frac{\partial \phi_i}{\partial t} = -L\frac{\delta \Omega}{\delta \phi_i}, \text{where } i = b, 1, \ldots, N \tag{6a}$$

$$\frac{\partial \mu_g}{\partial t} = \frac{1}{\chi_g}\left[\nabla \cdot \left(D_g \chi_g \nabla \mu_g\right) + S_g - \sum\nolimits_{i=0}^{N} \frac{\partial \rho_g}{\partial \eta_i}\frac{\partial \eta_i}{\partial t}\right] \tag{6b}$$

$$\frac{\partial \mu_v}{\partial t} = \frac{1}{\chi_v}\left[\nabla \cdot \left(D_v \chi_v \nabla \mu_v\right) + S_v - \sum\nolimits_{i=0}^{N} \frac{\partial \rho_v}{\partial \eta_i}\frac{\partial \eta_i}{\partial t}\right], \tag{6c}$$

where L is the order parameter mobility and Ω is the total grand potential; for j either v or g, D_j is the diffusion coefficient, χ_j is the susceptibility, S_j is the spatially varying source term, and ρ_j is the defect density. The densities $\rho_j = c_j/V_a$, where V_a is the atomic volume of UO_2. The diffusion coefficient for both vacancies and gas atoms should be faster along GBs and surfaces than through the bulk, however currently we assume that the diffusion coefficient is equal throughout the microstructure.

The total grand potential Ω is formulated from approximations of the grand potential density in the bubbles and grains, as well as numerical functions that provide an energetic driving force for only one order parameter to be equal to one at a given spatial location:

$$\Omega = \int_V \left(m\left[\sum\nolimits_{i=0}^{N}\left(\frac{\phi_i^4}{4} - \frac{\phi_i^2}{2}\right) + \sum\nolimits_{i=0}^{N}\sum\nolimits_{j\neq i}^{N}\frac{\gamma_{ij}}{2}\phi_i^2\phi_j^2 + \frac{1}{4}\right] + \frac{\kappa}{2}\sum\nolimits_{i=0}^{N}\left|\nabla\phi_i\right|^2 + h_{UO_2}\omega_{UO_2} + h_b\omega_b\right)dV \tag{7}$$

where m is a scalar weight, γ_{ij} allows for the adjustment between GB and surface energies, κ is the gradient energy coefficient, ω_{UO_2} and ω_b are the grand potential densities for UO_2 and bubbles, respectively, and h_{UO_2} and h_b are the corresponding switching functions. The switching functions interpolate between the properties of the UO_2 and bubble phases and are defined as:

$$h_{UO_2} = \frac{\sum_{i=1}^{N}\phi_i^2}{\sum_{i=0}^{N}\phi_i^2} \tag{8a}$$

$$h_b = \frac{\phi_0^2}{\sum_{i=0}^{N} \phi_i^2}. \tag{8b}$$

The grand potential densities are:

$$\omega_{UO_2} = f_{UO_2} - \mu_v \rho_v - \mu_g \rho_g \tag{9a}$$

$$\omega_b = f_b - \mu_v \rho_v - \mu_g \rho_g, \tag{9b}$$

where f_{UO_2} and f_b are the Helmholtz free energies of UO_2 and the bubbles, respectively. Both free energies are approximated as parabolic functions of the vacancy and gas atom concentrations, using the form

$$f_j = \frac{1}{2} k_g^j \left(c_g - c_g^{j,eq} \right)^2 + \frac{1}{2} k_v^j \left(c_v - c_v^{j,eq} \right)^2, \tag{10}$$

where j is either UO_2 or b, k_g^j and k_v^j are the polynomial coefficients, and $c_g^{j,eq}$ and $c_v^{j,eq}$ are the equilibrium concentrations. The susceptibilities are calculated as:

$$\chi_g = \frac{h_{UO_2}}{V_a^2 k_g^{UO_2}} + \frac{h_b}{V_a^2 k_g^b} \tag{11a}$$

$$\chi_v = \frac{h_{UO_2}}{V_a^2 k_v^{UO_2}} + \frac{h_b}{V_a^2 k_v^b}. \tag{11b}$$

The model parameters that impact the interface can be defined in terms of the interfacial width and the GB energy as:

$$\gamma_{ij} = 1.5, \text{where } i \neq j, i > 0, j > 0 \tag{12a}$$

$$\gamma_{0i} = \gamma_{i0} = 0.922, \text{where } i > 0 \tag{12b}$$

$$\kappa = \frac{3}{4} \sigma_{GB} l \tag{12c}$$

$$m = \frac{6\sigma_{GB}}{l}, \tag{12d}$$

where σ_{GB} is the GB energy. Table 1 lists the parameter values used in all of the simulations in this work. In UO_2, the diffusion coefficient of vacancies is much larger than that of Xe gas (Matthews et al., 2020); but the Xe diffusion is the limiting step for gas bubble behavior. However, we currently assume that the diffusion coefficient of vacancies is equal to that of fission gas to improve the numerical convergence of the model, as has been done in previous work (Aagesen et al., 2019), but we will investigate the impact of that

Table 1 Parameters used in the MARMOT simulations, including the reference citation(s)

Parameter	Value	Reference
V_a	0.0409 nm^3	(Aagesen et al., 2019)
$c_g^{UO_2,eq}$	$\exp\left(\frac{-3eV}{k_bT}\right)$	(Aagesen et al., 2019)
$c_v^{UO_2,eq}$	$\exp\left(\frac{-3eV}{k_bT}\right)$	(Aagesen et al., 2019)
$c_g^{b,eq}$	0.454	(Aagesen et al., 2019)
$c_v^{b,eq}$	0.546	(Aagesen et al., 2019)
$k_g^{UO2} = k_v^{UO2}$	2.57×10^9 J/m^3	(Aagesen et al., 2019)
$k_g^b = k_v^b$	9.0×10^{10} J/m^3	
σ_{GB}	1.5 J/m^2	(Nerikar et al., 2011)
l	480 nm	
D_g	0.0064 nm^2/s (1000 K) 2.3 nm^2/s (1800 K)	(Turnbull et al., 1982)
L	1.254×10^{-16} m/(J s) (1000 K) 1.96×10^{-14} m /(J s) (1800 K)	
S_v	$4s_g$	
y_1	0.25	
$y(0)$	9.1816×10^{-4} 1/s	(Setyawan et al., 2018)
a_1	0.949×10^{-4} 1/s	(Setyawan et al., 2018)
b_1	0.0703 1/nm	(Setyawan et al., 2018)
b_2	0.0371 1/nm	(Setyawan et al., 2018)
c	7.982 1/nm^2	(Setyawan et al., 2018)

assumption in future work. We make a similar assumption for the equilibrium concentration in UO_2. We also currently assume that GBs and bubble surfaces have the same order parameter mobility L and its value is set high enough to ensure that the bubble kinetics are controlled by the diffusion coefficient D_g. We calibrated the values for L for 1000 K and 1800 K to ensure diffusion control at the two temperatures used throughout this work.

The PDEs defining the evolution of the order parameters and chemical potentials are solved using the finite element method (FEM) with implicit time integration in the MARMOT mesoscale fuel performance code (Tonks et al., 2012). MARMOT is based on the Multiphysics Object-Oriented Simulation Environment (MOOSE) (Gaston et al., 2009; Schwen et al., 2017; Permann et al., 2020), which uses the PETSc library (Balay et al., 2020) for solving the system of nonlinear equations. The computational cost of polycrystalline simulations is reduced by using the grain tracker system available in MOOSE (Permann et al., 2016), which uses each order parameter $\phi_{i>1}$ to represent multiple grains. When two distinct grains that are represented by the same order parameter get close to each other, one is remapped to another order parameter to avoid non-physical grain coalescence.

Numerical code coupling of Xolotl (cluster dynamics) and MARMOT (phase field)

We couple Xolotl and MARMOT to create a hybrid mesoscale fission gas model that uses cluster dynamics to represent the behavior of fission gas within the grains and MARMOT to represent the behavior of fission gas on GBs, as depicted in Fig. 1. Xolotl models the generation of gas atoms due to fission, their diffusion through the UO_2 matrix, the clustering of the gas atoms, and their re-solution due to radiation damage. When gas atoms reach the locations of GBs or phase field bubble surfaces, Xolotl passes the gas arrival rate

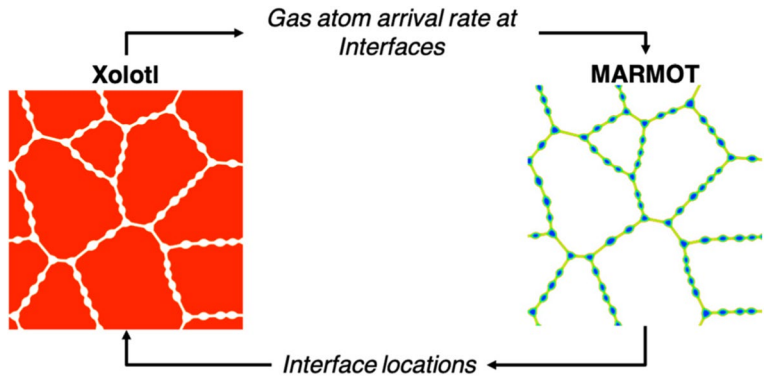

Fig. 1 Schematic of the coupling between the Xolotl and MARMOT codes, where Xolotl models the clustering and transport of gas atoms within the grains and MARMOT models bubble growth and coalescence on GBs, as well as GB migration. Xolotl passes the arrival rate of gas atoms reaching GBs and GB bubble surfaces to MARMOT, while MARMOT passes the interface locations to Xolotl

to MARMOT. The only source of gas atoms in MARMOT is the gas passed by Xolotl at these interfaces, such that they are the only locations at which the gas source term $S_g \neq 0$. Mobile gas atoms can arrive at the GB due to diffusion; immobile gas atom clusters reach the interfaces when the interfaces migrate to their location. MARMOT models the evolution of the interfaces due to GB migration, as well as the growth and coalescence of the GB bubbles. It passes the evolving locations of these interfaces back to Xolotl.

Both codes solve systems of PDEs using implicit time integration and both codes use PETSc (Balay et al., 2020) to solve the resultant systems of nonlinear equations. Xolotl uses FDM to discretize the simulation domain while MARMOT uses FEM. Thus, both codes discretize the simulation domain with a grid of points; however, Xolotl directly evaluates residuals at these points, while MARMOT evaluates residuals at the integration points in order to determine the nodal quantities. Monolithically coupling the solutions of two codes is difficult since each code generates its own nonlinear algebraic system of equations. For this reason, we employ a weak coupling in which, at a given time step, MARMOT solves its system of equations and passes the new interface locations to Xolotl. Xolotl then solves its system of equations and passes the rate at which gas atoms arrive at the interfaces S_g to MARMOT. Both codes then move on to the next time step.

The data exchange between the two codes is managed using the MultiApp and Transfer systems from the MOOSE framework (Gaston et al., 2015). In the coupled code, MARMOT is the master App and couples to Xolotl as a subApp, as illustrated in Fig. 2. An intermediate wrapper App is created to couple to the external Xolotl code. This

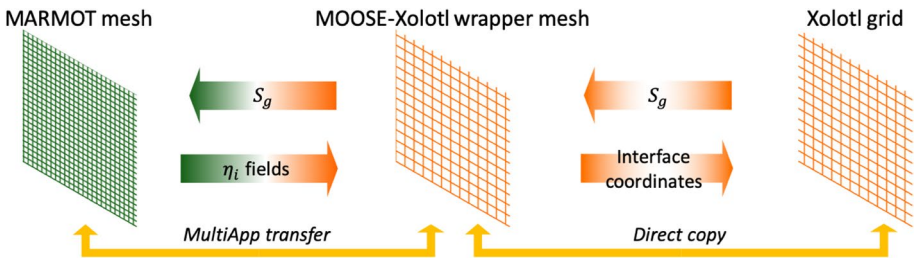

Fig. 2 Schematic of the data transfer approach used in the hybrid code

MOOSE-Xolotl wrapper App is a native MOOSE application that has an FEM mesh whose nodes are in the same locations as the Xoltol grid points. The data exchange between the wrapper App and Xolotl is implemented by a direct copy since both sides have the same solution vectors. The MultiApp Transfer system is employed to move data between MARMOT and the wrapper App. More precisely, the fission gas arrival rate at the interfaces S_g is directly copied from the Xolotl grid to the wrapper mesh and the interface coordinates are directly copied from the wrapper mesh to the Xolotl grid. A Transfer is used between the wrapper and MARMOT mesh in which the data from the wrapper mesh nodes are interpolated using the FEM basis functions to the nodes in the MARMOT mesh; S_g is transferred from the wrapper mesh to the MARMOT mesh and the order parameter fields ϕ_i are transferred from the MARMOT mesh to the wrapper mesh. The MARMOT and wrapper meshes can be different, allowing the MARMOT phase field calculations to take advantage of mesh adaptivity and have a finer mesh resolution at the interfaces. Note that the MARMOT mesh is never coarser than the wrapper mesh. This approach also works with a distributed mesh for large parallel computations. The MARMOT and Xolotl time steps do not have to be identical, although the MARMOT time steps must always be larger than or equal to the Xolotl times steps. When the Xolotl time steps are smaller than the MARMOT time steps, Xolotl takes multiple time steps without passing data and then takes a small time step to reach the MARMOT time and pass data.

Currently, Xolotl only includes gas atom clusters and, therefore, can only pass the gas atom arrival rate at the interfaces S_g. However, MARMOT evolves both gas atoms and uranium vacancies. Thus, we must assume some arrival rate for vacancies. When Xe diffuses through UO_2, it resides in a defect cluster containing multiple U vacancies; at high temperatures during reactor operation Xe moves with two U vacancies, while at intermediate temperatures it moves with four U vacancies (Matthews et al., 2020). We currently assume that four vacancies arrive with each gas atom such that the production rate of vacancies $S_v = 4S_g$ throughout the MARMOT domain for all temperatures. This is because even when Xe is moving in a smaller vacancy cluster, there are still vacancies being produced throughout the material that tend to segregate to grain boundaries and arrive separate from the Xe atoms. In the future, Xolotl will be expanded to consider clustering of vacancies and gas atoms and both S_g and S_v will be passed from Xolotl to MARMOT.

Model comparison

We ensure that the coupling between MARMOT and Xolotl is functioning correctly by comparing results from the hybrid model to a simulation only using the MARMOT phase field model. If clustering and re-solution of gas atoms is not included in Xolotl, then the spatially-resolved cluster dynamics model becomes identical to a solution of the diffusion equation. Thus, a simulation of the hybrid model without clustering or re-solution should yield identical results, within expected numerical differences between the two solution methods, to a stand-alone MARMOT simulation in which fission gas is produced uniformly throughout the domain.

For the comparison, we simulate a $20\,\mu m \times 20\,\mu m$ two-dimensional (2D) domain with periodic boundary conditions containing five grains represented with five order

parameters (MOOSE's grain tracker is not used for these simulations). There are 14 initial bubbles with a radius of 0.73 μm positioned randomly along the GBs. These initial bubbles are not representative of fresh fuel but are used here to test the model. The simulations are carried out with a fission rate density of 1.09×10^{19} fissions $m^{-3}s^{-1}$. The MARMOT phase field model, in both simulations, used the parameter values previously listed in Table 1. The simulations are carried out for 1.2×10^8 s (1389 days) at 1800 K. The mesh used in both codes is identical, and consisted of 126 by 126 nodes. Figures 3(b) and (c) compare the results predicted from the stand-alone and coupled version of MARMOT, respectively, and indicate a similar qualitative result. A quantitative comparison between the bubble fraction evolution indicates only a slight deviation over time (Fig. 3d), with a maximum difference of less than 1% that is well within the expected differences between FDM and FEM. These results indicate that the coupling algorithm accurately passes fission gas between the models, without artificially loosing or gaining gas, and that the hybrid model functions well.

Having ensured that the hybrid model is performing as expected, we can also use the results from the hybrid model to illustrate its general features. Figure 4(a) shows snapshots in time of the intragranular gas fraction computed by Xolotl, Fig. 4(b) of the gas atom arrival rate at the interfaces computed by Xolotl and passed to MARMOT, and Fig. 4(c) of the GB gas fraction evolved by MARMOT. As seen in Fig. 4(a), the largest intragranular gas concentrations build up in the center of the grains, furthest away from the GBs. The larger grains have a higher concentration of the mobile Xe atoms due to the longer diffusion distance to the GB. The magnitude of the concentrations eventually reaches steady state, once the flux of single Xe atoms to the GBs is equal to their generation due to fission and once the GBs stop migrating. These results do not include clustering, so all produced gas is mobile and is free to diffuse to the GBs. If clustering were included, some Xe atoms would be trapped in immobile clusters. This behavior will be discussed more in Section 4. The gas atom arrival rates (see Fig. 4(b)) are heterogeneous across the interfaces, and their value adjust as the GBs migrate and the bubbles grow. They are the largest at interfaces that are migrating, since they pick up diffusing Xe atoms and Xe atoms already at the new interface location. Due to the arrival of gas atoms to the GBs, the intergranular bubbles grow and interconnect, as shown in Fig. 4(c). The bubbles interact with the GBs and restrict their migration. New bubbles form as the Xe concentrations along the GBs increase. MARMOT has only a small concentration of Xe within the grains, since the source term is only nonzero at the interfaces and it is more energy favorable for Xe to be within GB bubbles than within grains.

Computational performance

The hybrid fission gas model provides a powerful capability to combine the physics represented by the cluster dynamics and phase field methods. It has also been created to leverage the powerful parallel computing capabilities of the Xolotl and MARMOT codes to enable it to take advantage of high-performance computing clusters. The two codes have been loosely coupled such that the parallel scaling of each code is unchanged. In addition, the data passed between the codes is distributed across processes to make the

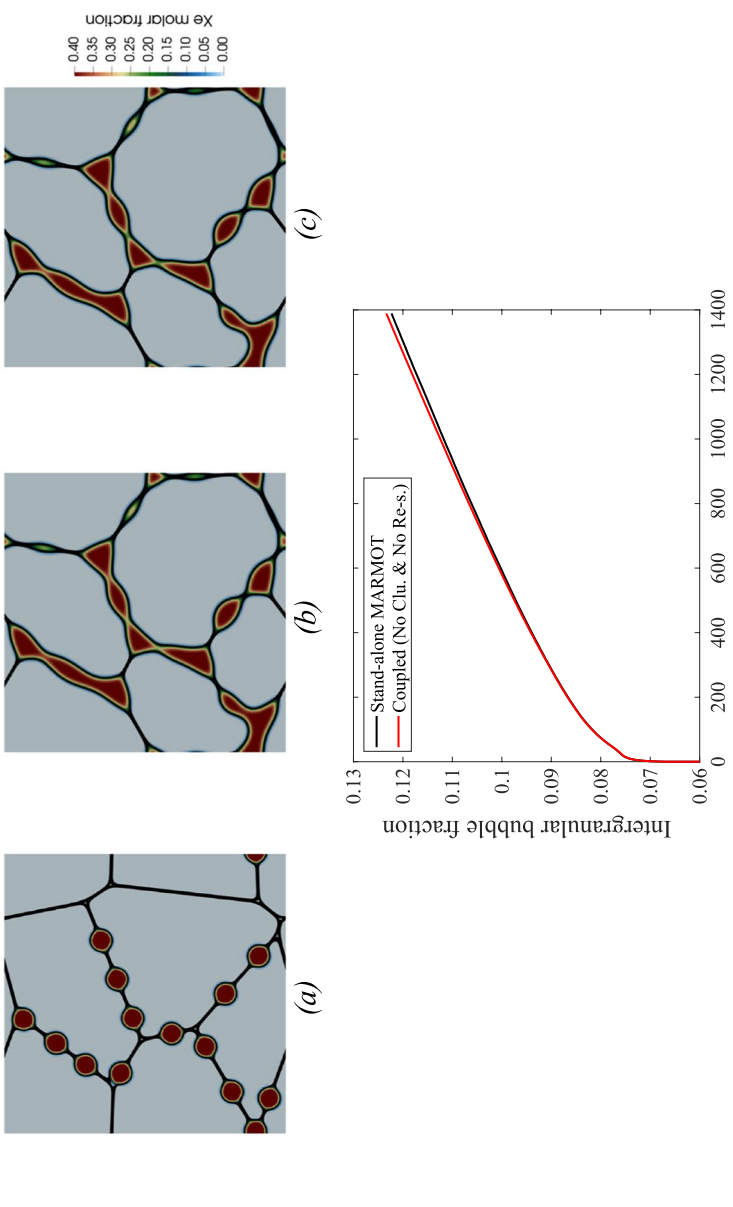

Fig. 3 Investigation of the hybrid model coupling by comparing a simulation without clustering or re-solution with a stand-alone MARMOT simulation; (**a**) shows the initial microstructure; (**b**) and (**c**) show the final microstructure predicted by the stand-alone MARMOT simulation and the coupled simulation, respectively. They are shaded by the gas fraction and in (**c**) this includes the gas from both Xolotl and MARMOT. The interfaces are shown in black. (**d**) shows a plot of the intergranular bubble fraction versus time for the two simulations

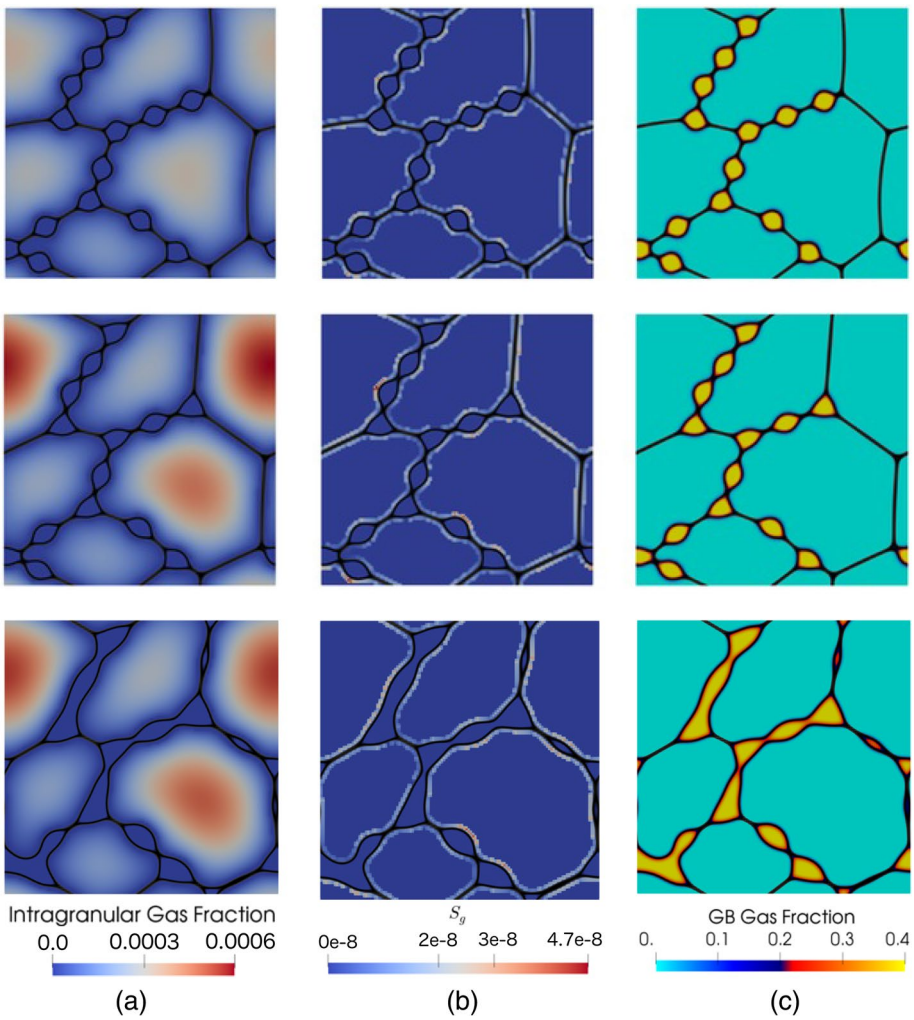

Fig. 4 Evolution of the microstructure over time predicted by the coupled model; (**a**) shows the intragranular gas fraction predicted by Xolotl; (**b**) shows the arrival rate of gas at the interfaces transferred from Xolotl to MARMOT; (**c**) shows the GB gas fraction predicted by MARMOT. In each, the top image shows the microstructure after 20 days, the middle image after 127 days, and the bottom image after 1389 days. The interfaces are shown in black

communication scale well. In this section, we demonstrate the computational performance of the hybrid model.

The computational performance has been assessed by investigating the computation time (the wall clock time required for the completion of simulations) using the domain used in the model comparison from the previous section (a $20\,\mu m \times 20\,\mu m$ domain with periodic boundary conditions containing five grains and 14 initial bubbles and resolved with 126×126 nodes). As in the previous section, we do not use grain tracker. Specifically, we compare the portion of the total wall time taken up by MARMOT, Xolotl, and the data transfer between the codes. We also compare the wall time as a function of the number of processes used for the computation. We consider the timing for three different approaches to modeling the intragranular fission gas behavior with Xolotl: a case with no clustering nor re-solution (similar to that

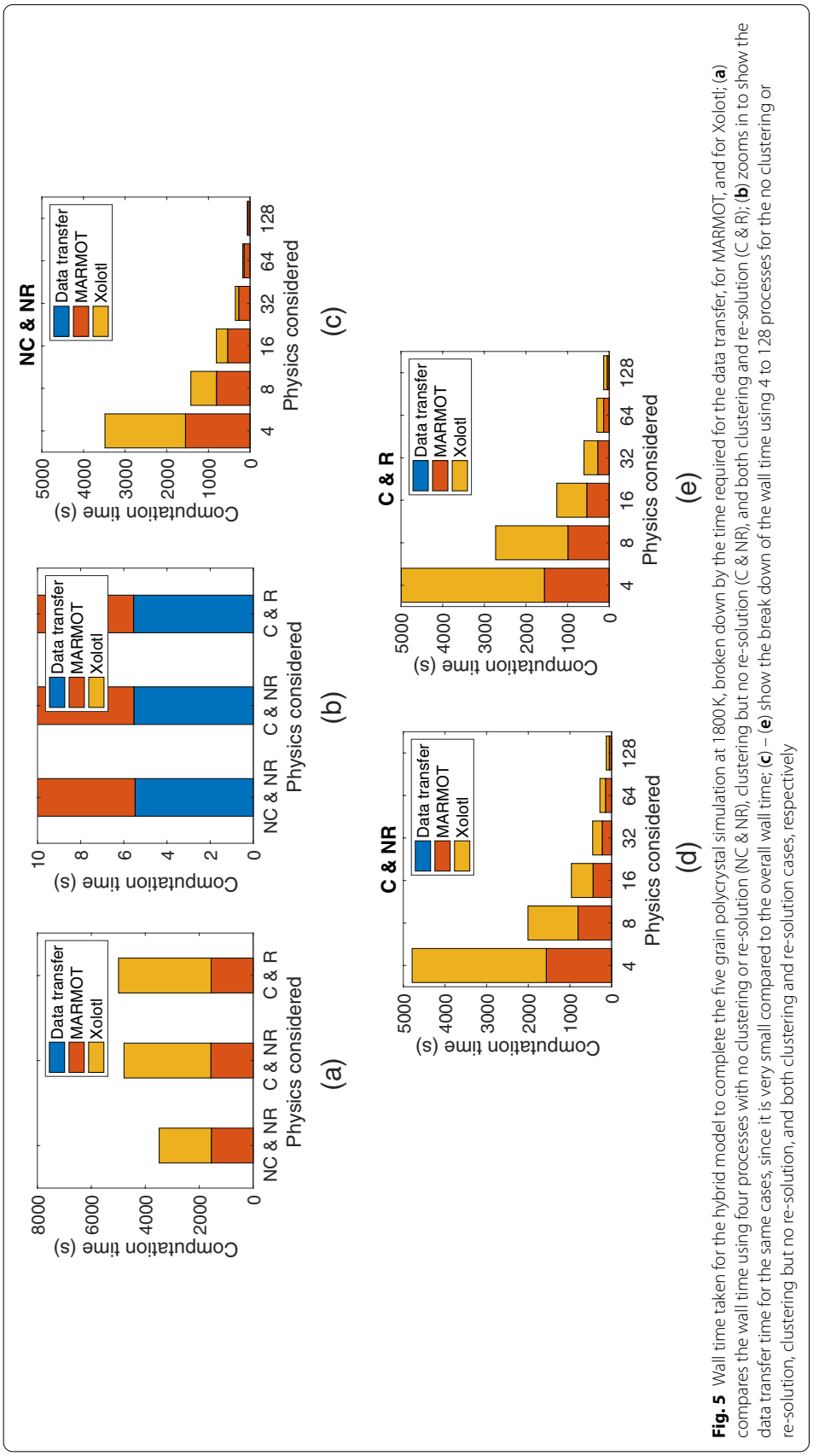

Fig. 5 Wall time taken for the hybrid model to complete the five grain polycrystal simulation at 1800 K, broken down by the time required for the data transfer, for MARMOT, and for Xolotl; (**a**) compares the wall time using four processes with no clustering or re-solution (NC & NR), clustering but no re-solution (C & NR), and both clustering and re-solution (C & R); (**b**) zooms in to show the data transfer time for the same cases, since it is very small compared to the overall wall time; (**c**) – (**e**) show the break down of the wall time using 4 to 128 processes for the no clustering or re-solution, clustering but no re-solution, and both clustering and re-solution cases, respectively

used in the model comparison), a case with clustering but no re-solution, and a case with clustering and re-solution. The simulations were carried out on the Falcon cluster at Idaho National Laboratory (INL). Each node is comprised of 36 processor cores, 128GB DRAM, with a FDR InfiniBand (56 GB/s) interconnect. The system runs SUSE Linux, and Xolotl and MARMOT were compiled with version gcc 5.5.0 of C/C++ compiler. The minimum configuration capable of running the test case was four processes. Simulations were run from 4 to 128 processes. The results are shown in Fig. 5.

When using four processes, the computation time for the hybrid model increased significantly from the case with no clustering nor re-solution to the case with clustering but no re-solution, as shown in Fig. 5(a); this is due to the large increase in the number of variables required to model the various gas atom clusters in Xolotl (1364 DoFs per grid point). There was a much smaller increase in the computation time with the addition of re-solution, since the re-solution model needs a larger network as the bubbles grow more rapidly than with clustering only (1888 DoFs per grid point). The computation time of the MARMOT portion of the simulations was unchanged in the three cases, since the differential equations solved in MARMOT are similar regardless of the amount of gas being passed from MARMOT to Xolotl. With four processes, the cost of the two codes was approximately equal when neither clustering or re-solution was used, but once clustering was added, Xolotl took the majority of the computation time. The time required for data transfer between the codes was very small compared to the overall cost, and cannot even be seen in Fig. 5(a). Figure 5(b) shows just the cost of the data transfer on its own, which was on the order of 0.1% of the total computation cost.

The total computation cost for the three cases when the number of processes is increased from four to 128 is shown in Figs. 5(c) – (e). The cost of the data transfer between the codes was negligible for all numbers of processes. However, as the number of processes increased, MARMOT took a larger and larger portion of the overall computation time, indicating that Xolotl has better parallel scaling than MARMOT at present. Thus, we anticipate future effort to further optimize the scaling of MARMOT.

To more accurately assess the parallel scalability of the coupled code, we performed both a strong and weak scaling study using the three cases discussed above. For the strong scaling study, the same simulation domain was used as above; however, we used a finer mesh in both codes (201×201 nodes). The time step was fixed to 0.5 s and 20 total time steps were simulated. We performed six simulations, using from 4 to 128 processes. For the weak scaling study, we increased the number of nodes as we increased the number of processes, to keep the ratio of DoFs per process constant. We used 201×201 nodes with four processes, 401×401 nodes for 16 processes, and so on up to 1001×1001 nodes with 100 processes.

Figure 6 presents the results of the two scaling studies. The scaling for a stand-alone MARMOT simulation is shown for reference. For both studies, we show the relative speedup of the simulations with respect to the four-process simulation versus the increasing numbers of processes. Ideally in strong scaling, when the number of processes doubles the speedup would also double. The hybrid model scaled extremely well (Fig.6(a)), staying at or above ideal scaling. The coupled code scaled slightly better than the stand-alone MARMOT simulation since it had more DoFs. The coupled code with no clustering or re-solution demonstrated super-linear scaling, likely because the

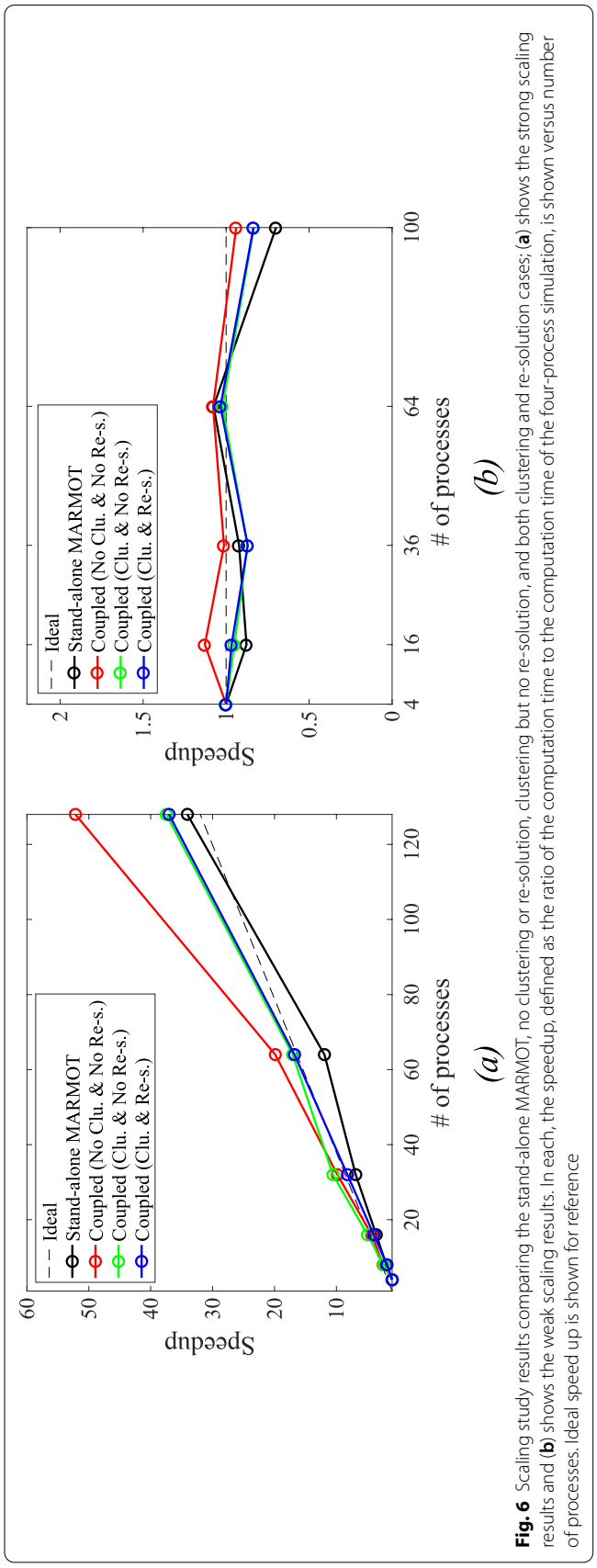

Fig. 6 Scaling study results comparing the stand-alone MARMOT, no clustering or re-solution, clustering but no re-solution, and both clustering and re-solution cases; (**a**) shows the strong scaling results and (**b**) shows the weak scaling results. In each, the speedup, defined as the ratio of the computation time to the computation time of the four-process simulation, is shown versus number of processes. Ideal speed up is shown for reference

problem fit better into the physical memory at the higher number of processes. Ideally in weak scaling, the speedup stays at one as the number of processes increases. The weak scaling results (Fig. 6(b)) were worse than the strong scaling results, but still reasonable. Though the performance was below ideal, it did not vary significantly as the number of processes increased from 4 to 100.

Results

Having ensured that the coupling between codes in the hybrid model is performing well and having assessed its computational performance, we now use the hybrid model to investigate fission gas behavior under various conditions. We first investigate the impact of the intragranular physics on the fission gas behavior, we then investigate the impact of the temperature, and we end by investigating the impact of the grain size. In all cases, we model a $20\,\mu m \times 20\,\mu m$ 2D UO_2 polycrystal with a fission rate density of 8.0×10^{18} fissions $m^{-3}s^{-1}$ and eight initial 0.5 µm radii Xe bubbles randomly located on GBs. The initial bubbles are included to avoid the need to represent GB bubble nucleation with the phase field model. Due to the initial bubbles, the initial condition is representative of fuel that has already experienced some fission rather than fresh fuel. For all these simulations, we use MOOSE's grain tracker feature to decrease the computational cost of modeling ten or more grains.

Impact of intragranular physics

The hybrid model can simultaneously predict the production, migration, clustering, and re-solution of fission gas atoms within the grains and predict the migration of GBs and the evolution of the GB bubbles. The behavior within the grains and on GBs are coupled and changes in one will have large impacts on the other. In this section, we investigate the impact of changes in the intragranular physics on the overall fission gas behavior.

In each simulation, we model a 2D UO_2 polycrystal with ten initial grains, as shown in Fig. 7(a). The fuel temperature is 1800 K. We compare the behavior with no clustering and no-resolution, clustering but no re-solution, and clustering with re-solution. The final microstructures are shown in Figs. 7(b) – (d). We also plot the bubble fraction over time and the fraction of the total Xe that is within the grains over time in Figs. 7(e) and (f).

When clustering is not considered in the hybrid model, all fission gas produced within the grains will eventually migrate and arrive at the GBs. This results in the rapid growth of the initial intergranular bubbles and even the formation of new intergranular bubbles at triple junctions and eventually between triple junctions, as shown in Fig. 7(b). Some GB migration also occurs, but not much (the number of grains goes from ten to nine), as the bubbles resist the GB migration. The intergranular bubble fraction grows quickly, as shown in Fig. 7(f). Similar behavior has been shown in other works that have used phase field or related methods to model intergranular fission gas bubbles in UO_2 (Aagesen et al., 2019; Prudil et al., 2019; Prudil et al., 2020). However, this behavior does not consider the clustering of gas atoms that occurs within the grains, and therefore will overestimate the growth of the intergranular bubbles.

When the hybrid model includes xenon clustering and fission gas bubble formation, very different behavior is predicted. A large fraction of the fission gas produced

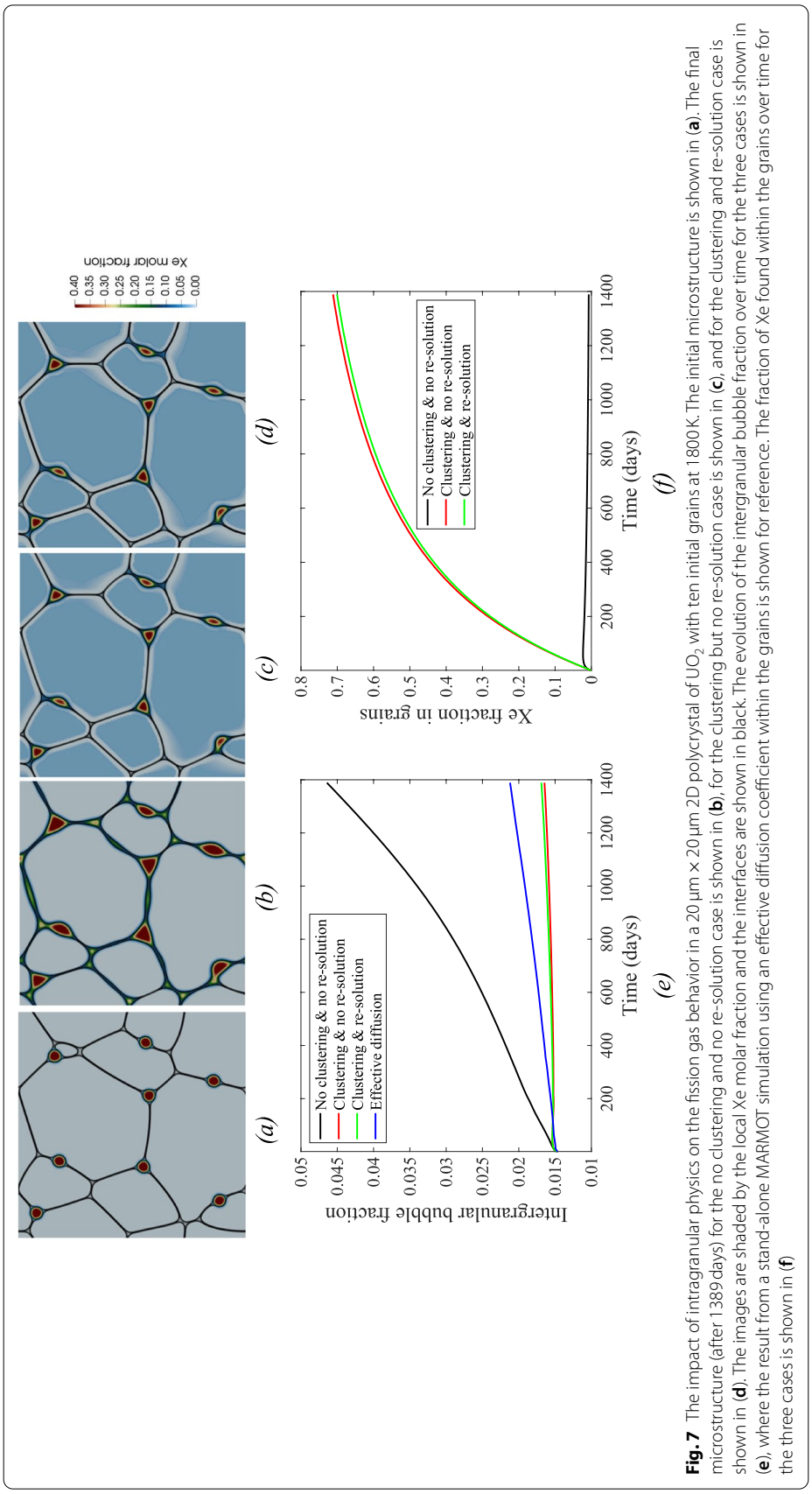

Fig. 7 The impact of intragranular physics on the fission gas behavior in a 20 μm × 20 μm 2D polycrystal of UO_2 with ten initial grains at 1800 K. The initial microstructure is shown in (**a**). The final microstructure (after 1389 days) for the no clustering and no re-solution case is shown in (**b**), for the clustering but no re-solution case is shown in (**c**), and for the clustering and re-solution case is shown in (**d**). The images are shaded by the local Xe molar fraction and the interfaces are shown in black. The evolution of the intergranular bubble fraction over time for the three cases is shown in (**e**), where the result from a stand-alone MARMOT simulation using an effective diffusion coefficient within the grains is shown for reference. The fraction of Xe found within the grains over time for the three cases is shown in (**f**)

within the grains clusters to form immobile intragranular bubbles. Since only the single Xe atoms are mobile, a much smaller amount of gas arrives at the GBs. Thus, as shown in Fig. 7(c), more Xe is found within the grains and the existing bubbles have grown much less than in the case without clustering and no additional GB bubbles have formed. The growth rate of the intergranular bubble fraction decreases by a factor of six (Fig. 7(e)). The inclusion of re-solution in the hybrid model results in some of the gas being knocked out of the intragranular bubbles to form additional mobile Xe monomers. This results in a small increase in the growth rate of the intergranular bubble fraction over the case with clustering but no re-solution. The final microstructure is similar to the case with clustering and no re-solution, but with slightly larger intergranular bubbles (Fig. 7(d)). As a reference case, we also run a stand-alone MARMOT simulation in which we use the effective diffusion coefficient (as defined and parameterized in Pastore et al. (Pastore et al., 2013)) within the grains to approximate the impact of clustering and re-solution, and its predicted intergranular bubble fraction is also shown in Fig. 7(e). The MARMOT simulation using the effective diffusion coefficient has a much slower increase in the intergranular bubble fraction than the hybrid model case without clustering. However, it is still faster than predicted by the full hybrid model. This likely due to the different re-solution models implemented in the effective diffusion parameterization from Pastore et al. (Pastore et al., 2013) and in the cluster dynamics model (taken from (Setyawan et al., 2018)).

To better understand the drastic change in the growth rate of the intergranular bubbles, we also plot the fraction of Xe within the grains over time, as shown in Fig. 7(f). All of the simulations begin with a fraction of zero, as there is no initial Xe in the grains. This fraction increases over time, and it initially increases at the same rate for all three cases. However, in the case with no clustering, the fraction quickly stops increasing as the Xe atoms diffuse to the GBs and enter the intergranular bubbles. The fraction slowly decreases for the rest of the simulation, as the intergranular bubbles grow and new bubbles form, decreasing the diffusion distance to the bubbles. In the two cases with clustering, the fraction of Xe within the grains continues to increase throughout the simulation, as more and more of the gas is trapped within immobile intragranular bubbles. After 1389 days, more than 70% of the Xe present in the material is trapped within the grains. The fraction is slightly smaller for the case with re-solution, due to the increase in Xe monomer concentration resulting from Xe emission from the intragranular bubbles, and this higher monomer concentration can diffuse to the GBs. Thus, intragranular bubble formation has an enormous impact on the intergranular bubble growth, since the majority of the Xe never arrives at the GBs.

As described in Section 2.3, in the hybrid model four times as many vacancies arrive at the interfaces as gas atoms. However, the equilibrium concentration of vacancies within bubbles is only 20% larger than the gas atoms, as shown in Table 1. Thus, there are always excess vacancies in the system that are not included in the bubbles. In all the simulations described above, these excess vacancies move into the grains and along GBs. The molar fraction of vacancies within the grains gets as high as 6×10^{-4} and on GBs as high as 8×10^{-4}. These excess vacancies ensure that the bubble behavior is controlled by the gas atom behavior, as vacancies are always available if needed.

Impact of temperature

There is a large temperature gradient in UO_2 fuel pellets, with the temperature ranging from around 800 K at the pellet edge to around 1200 K at the pellet center during normal operation and as high as 1800 K during reactor transients. Due to the large impact of temperature on the fission gas diffusion rate, the fission gas behavior varies significantly across the radius of a fuel pellet. In this section, we use the hybrid model to compare the behavior in our initial 2D polycrystal (see Fig. 7(a)) at 1800 K, from the previous section, with the behavior at 1000 K. We compare the behavior when considering clustering but no re-solution and with both clustering and re-solution. The 1800 K results are identical to those shown in the previous section.

At 1000 K, the microstructure does not evolve as it does at 1800 K (see 8(a) and 8(b) for the 1000 K results and 8(c) and 8(d) for the 1800 K results). Both the GB mobility and the Xe diffusion coefficient are much smaller at 1000 K than at 1800 K, such that after 1389 days at 1000 K, almost no GB migration has occurred and all ten grains are still present. The shape of the intergranular bubbles has not changed either, such that they have not reached the lenticular (on GBs) and triangular (at triple junctions) shapes that they reach at 1800 K. More shape change would occur if we consider fast surface diffusion of vacancies. The intergranular bubble fraction increases much slower at 1000 K than at 1800 K, as shown in Fig. 8(e), since the Xe monomers diffuse slower towards the GBs. This results in an increase in the fraction of Xe within the grains, as shown in Fig. 8(f).

The impact of re-solution on the results appears to be smaller at 1000 K than at 1800 K from the results in Fig. 8. However, this is misleading since these results only compare gas within grains to that which has arrived at GBs. Figure 9 shows the spatial distribution of the Xe monomer concentration throughout the polycrystal for the two temperatures without and with re-solution. At 1000 K, re-solution results in a very large increase in the concentration of Xe monomers (an increase of twenty times); however, at 1800 K re-solution does not have this large effect. This large increase is due to the higher rate of re-solution from smaller fission gas bubbles than from larger bubbles predicted by the model from Setyawan et al. (Setyawan et al., 2018). The lower Xe diffusivity at 1000 K results in a larger density of small intragranular bubbles that maximizes the rate of Xe resolution. This increase in the xenon monomer concentration at 1000 K does not result in a large acceleration of the increase of the intergranular bubble fraction because the diffusion rate is so small. Thus, the fraction of Xe in the grains is similar between the cases with and without re-solution, as shown in Fig. 8(f), but less Xe resides in intragranular bubbles. Including re-solution at 1000 K causes the Xolotl calculation to be slower. Re-solution increases the cost of the hybrid model simulation by 50% more at 1000 K than at 1800 K, as a result of the smaller timestep necessitated by the reaction rate densities and the additional reaction terms in the re-solution model.

Impact of grain size

Fission gas release has been shown to decrease as the grain size increases (Turnbull, 1974). Thus, we investigated the impact of the initial grain size on the fission gas behavior. We again model the behavior of a 20 μm × 20 μm 2D polycrystal of UO_2 at 1800 K. However, now we compare the behavior in polycrystals with ten grains (identical to the results from Fig. 8), twenty grains, and thirty grains. These cases correspond to an

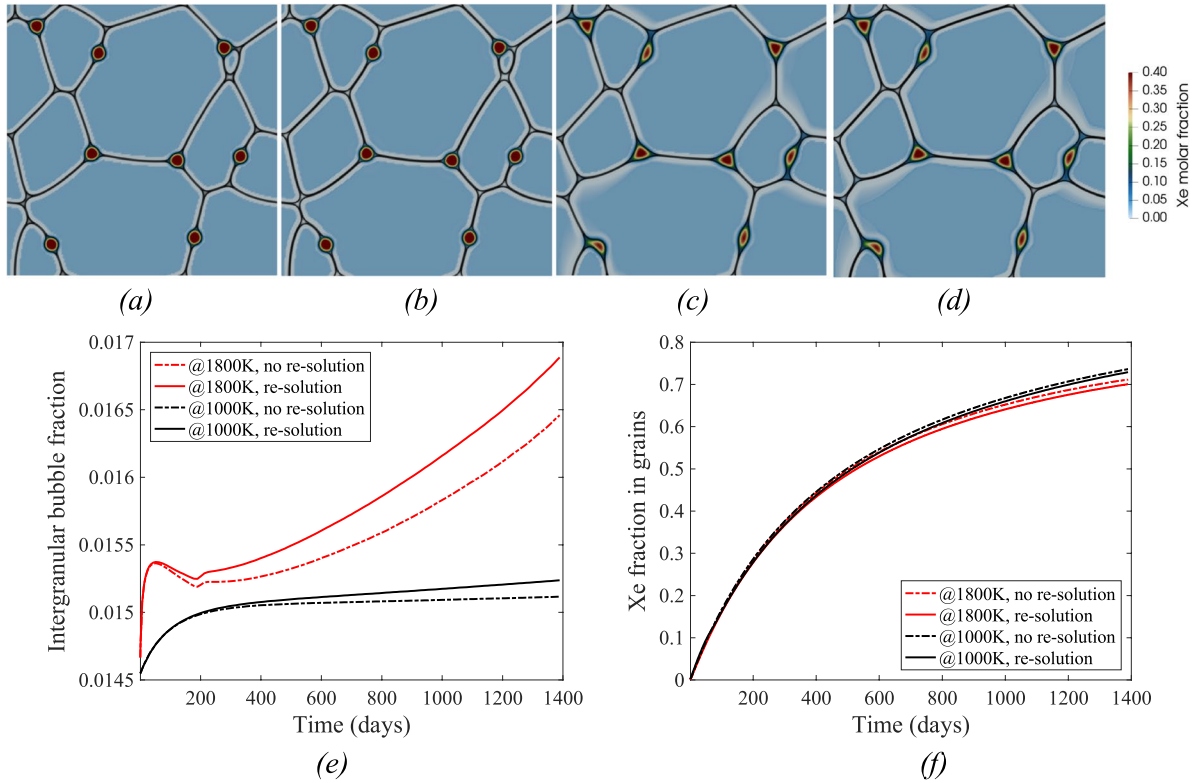

Fig. 8 The impact of temperature on the fission gas behavior in a 20 µm × 20 µm 2D polycrystal of UO_2 with ten initial grains. The final microstructure (after 1389 days) for the clustering but no re-solution case and for the clustering and re-solution case at 1000 K is shown in (**a**) and (**b**), respectively. The final microstructure for the clustering but no re-solution case and for the clustering and re-solution case at 1800 K is shown in (**c**) and (**d**), respectively. The images are shaded by the local Xe molar fraction and the interfaces are shown in black. The evolution of the intergranular bubble fraction over time for the two temperatures is shown in (**e**). The fraction of Xe found within the grains over time for the two temperatures is shown in (**f**)

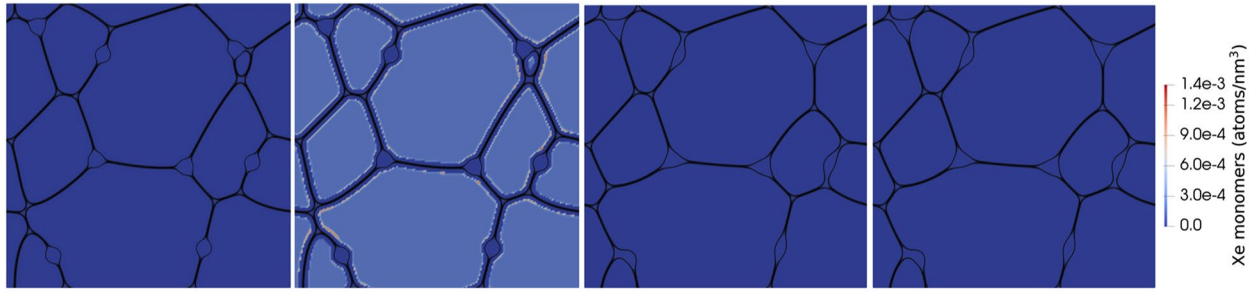

Fig. 9 The impact of re-solution on the Xe monomer concentration in a 20 µm × 20 µm 2D UO_2 polycrystal with 10 initial grains. The Xe monomer concentration throughout the polycrystal after 1389 days for the clustering but no re-solution case and for the clustering and re-solution case at 1000 K is shown in (**a**) and (**b**), respectively. The Xe monomer concentration for the clustering but no re-solution case and for the clustering and re-solution case at 1800 K is shown in (**c**) and (**d**), respectively. The interfaces are shown in black. Re-solution results in a large Xe monomer concentration at 1000 K, while it does not at 1800 K. The maximum Xe monomer concentration is 20 times smaller in (**a**), (**c**), and (**d**) than in (**b**) and is not visible in the images

average grain size of 7.1 µm, 5.0 µm, and 4.1 µm. Each polycrystal has eight initial 0.5 µm radii intergranular bubbles. We include clustering and re-solution in each simulation. It is important to note that the current phase field model in MARMOT assumes that the diffusion rate of Xe does not vary between the bulk, along GBs, and along surfaces, as stated in Section 2.2.

Figure 10 shows the simulation results for the cases with different grain size. Figures 10(a) – (c) show the evolution of the microstructure over time, Fig. 10(d) shows the evolution of the intergranular bubble fraction with time, and Fig. 10(e) shows the evolution of the fraction of gas within the grains. The amount of grain growth is much larger for the twenty and thirty grain simulations than for ten grains: the number of grains decreases from ten to nine (a 5% increase in grain size), from twenty to thirteen (a 24% increase in grain size), and from thirty to twenty (a 22% increase in grain

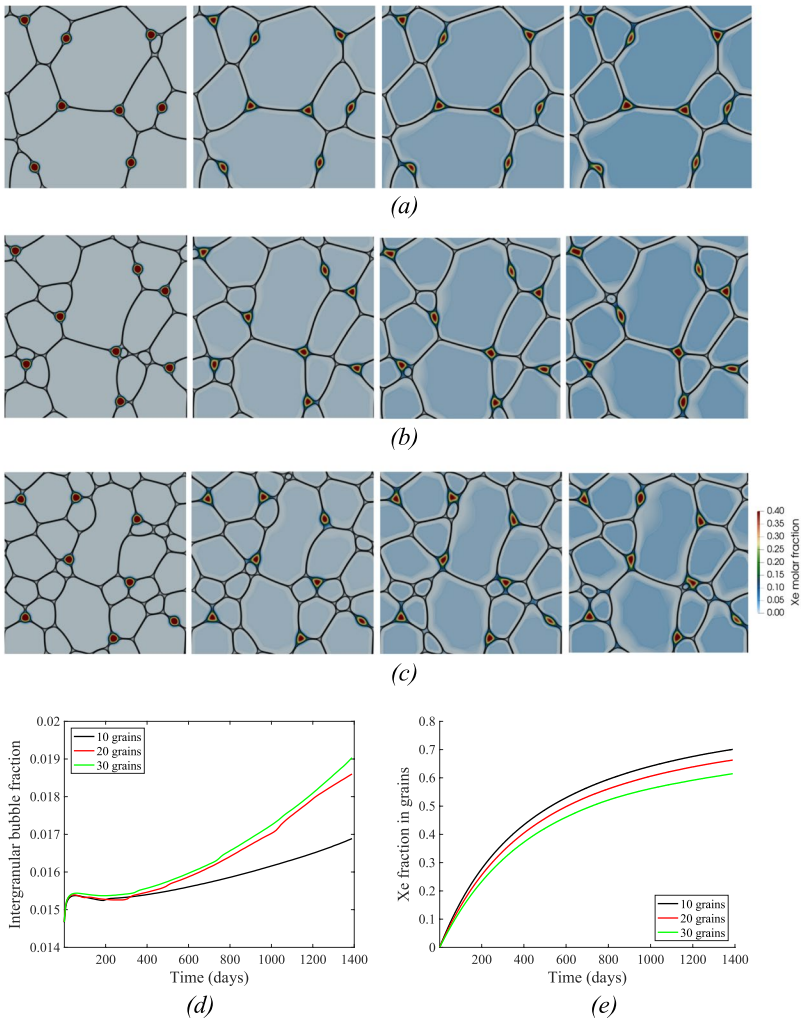

Fig. 10 The impact of initial grain on the fission gas behavior in a 20 µm × 20 µm 2D polycrystal of UO_2 at 1800 K with clustering and re-solution. The evolution of the grain structure and fission gas concentration over time are shown for the ten, twenty, and thirty grain cases in (**a**), (**b**), and (**c**), respectively. The four images correspond to t = 0, 336, 897, and 1389 days, from left to right. The evolution of the intergranular bubble fraction over time for the three cases is shown in (**d**). The fraction of Xe found within the grains over time for the three cases is shown in (**e**)

size). This increase in grain growth is due to the increase in the driving force with smaller grain size and to the decrease in the fraction of GBs that are pinned by the initial bubbles.

The increase in the intergranular bubble fraction with time is much faster in the cases with twenty and thirty initial grains than in the case with ten initial grains, as shown in Fig. 10(e). The increase in the intergranular bubble fraction is also faster in the case with thirty initial grains than in the case with twenty initial grains, but by a much smaller amount. In a real material, we would expect intergranular bubbles to grow faster in material with smaller grains due to an increase in the arrival rate of gas atoms to GBs and then fast diffusion along GBs to the intergranular bubbles. However, as stated above, in our model we currently neglect this effect. Therefore, this increase must be due to other factors. Figures 10(a) – (c) show the evolution over time of the intragranular Xe molar fraction. As the GBs migrate, they leave behind a region depleted of Xe gas as the GBs sweep up all of the Xe. This allows the GBs to obtain the mobile Xe monomers but also the gas from the immobile clusters. In the model, all gas on the GBs is mobile and can then diffuse to the intergranular bubbles. Since more GB migration occurs in the polycrystals with more grains, this results in more sweeping of the gas and thus a faster increase in the intergranular gas fraction. This is clearly shown in Figs. 10(a) – (c) by the fact that more depleted regions are evident in the simulations with more initial grains. Figure 10(f) shows that the amount of gas within the grains decreases with increasing number of grains (and thus decreasing grain size), due to this sweeping. Change in the fraction of Xe within the grains with the initial number of grains is more uniform than the change in the intergranular bubble fraction, and this is likely due to the fact that once the gas is swept up by the GBs, it still has to diffuse along the GBs to intergranular bubbles and that time is not very different in the twenty and thirty grain simulations. In future work, we will add fast GB diffusion to the model which will accelerate the arrive of the gas at GBs at the intergranular bubbles. These results show the importance of capturing GB migration in simulations of fission gas behavior.

Conclusions

This paper demonstrates the capabilities of our new hybrid model of fission gas behavior in UO_2 reactor fuel. A cluster dynamics model, implemented in the Xolotl code, is used to model the generation, diffusion, clustering and bubble formation, and re-solution of Xe atoms within the grains. It is coupled to a phase field model, implemented in MARMOT, which is used to model the diffusion of gas along the GBs, the growth and coalescence of intergranular bubbles, and GB migration. The two codes are loosely coupled, where MARMOT passes GB and intergranular bubble surface locations to Xolotl, and Xolotl passes the rate of gas arriving at those interfaces to MARMOT. We have ensured that the coupling is functioning correctly by comparing a result using only MARMOT to a result from the hybrid model that neglects clustering and re-solution. We have also shown that the hybrid model performs well computationally, with excellent parallel scaling.

We have used the hybrid model to investigate the impact of intragranular physics, temperature, and initial grain size on the fission gas behavior. Including fission gas clustering within grains to form small intragranular bubbles has a very large impact on the growth of the intergranular fission gas bubbles, as up to 70% of all

the fission gas is trapped within the grains. At 1800 K, including re-solution results in a slight decrease in the fraction of gas within the grains and a slight increase in the intergranular bubble fraction. At 1000 K, much less evolution takes place in the microstructure. The increase in the intergranular bubble fraction is much slower than at 1800 K and more gas is trapped within the grains. The impact of re-solution is higher at 1000 K than at 1800 K, resulting in a 20-times increase in the concentration of Xe monomers within the grains. Due to the slow diffusion, this does not translate to a significant increase in the growth of the intergranular bubbles. The growth of the intergranular bubble fraction accelerates as the initial grain size decreases. As we currently assume that fission gas diffuses at the same rate within the bulk and along GBs and surfaces, this acceleration with decreasing grain size is due to the sweeping up of immobile fission gas during GB migration. Thus, our hybrid model provides a powerful means of representing many of the critical physical phenomena that influence fission gas behavior. It can also provide critical insights on how to improve the effective diffusivity that is currently used in fission gas release models.

Abbreviations

2D: two-dimensional; DoFs: degrees of freedom; FDM: finite difference method; FEM: finite element method; GB: grain boundary; INL: Idaho National Laboratory; Kr: krypton; LANL: Los Alamos National Laboratory; MOOSE: Multiphysics Object-Oriented Simulation Environment; PDE: partial differential equation; SciDAC: Scientific Discovery through Advanced Computing; UO2: uranium dioxide; Xe: xenon.

Acknowledgements

Not applicable.

Authors' contributions

MRT, DA, and BDW designed the study. DK, SB, DEB, and MRT produced and analyzed the data. DK, SB, PR, and FK developed the software used in this study. DK, SB, and MRT prepared the draft. DK, DEB, FK, DA, MRT, and BDW revised the draft. All authors read and approved the final manuscript.

Funding

This material is based upon work supported by the U. S. Department of Energy, Office of Nuclear Energy and Office of Science, Office of Advanced Scientific Computing Research through the Scientific Discovery through Advanced Computing (SciDAC) project on Simulation of Fission Gas through the grant DOE DE-SC0018359 at the University of Tennessee.

This research made use of the resources of the High-Performance Computing Center at Idaho National Laboratory, which is supported by the Office of Nuclear Energy of the U.S. Department of Energy and the Nuclear Science User Facilities under Contract No. DE-AC07-05ID14517.

This work was performed in part at Los Alamos National Laboratory (LANL). Los Alamos National Laboratory, an affirmative action/equal opportunity employer, is operated by Triad National Security, LLC, for the National Nuclear Security Administration of the U.S. Department of Energy under Contract No. 89233218CNA000001. It was also performed in part at Oak Ridge National Laboratory, managed by UT-Battelle, LLC for the U.S. Department of Energy under Contract No. DE-AC05-00OR22725, and at Idaho National Laboratory, managed by Battelle Energy Alliance, LLC under Contract No. DE-AC07-05ID14517 with the U.S. Department of Energy.

Availability of data and materials

The datasets generated during and/or analyzed during the current study are available from the corresponding author on reasonable request.

Declarations

Competing interests

The authors declare that they have no competing interests.

Author details

[1]University of Florida, Gainesville, FL, USA. [2]University of Tennessee, Knoxville, TN, USA. [3]Oak Ridge National Laboratory, Oak Ridge, TN, USA. [4]Idaho National Laboratory, Idaho Falls, ID, USA. [5]Los Alamos National Laboratory, Los Alamos, NM, USA.

Received: 1 June 2021 Accepted: 28 October 2021
Published online: 27 January 2022

References

L.K. Aagesen, D. Andersson, B.W. Beeler, M.W.D. Cooper, K.A. Gamble, Y. Miao, G. Pastore, M.R. Tonks, Phase-field simulations of Intergranular fission gas bubble behavior in U3Si2 nuclear fuel. J. Nucl. Mater. **541**, 152415 (2020)
L.K. Aagesen, D. Schwen, M.R. Tonks, Y. Zhang, Phase-field modeling of fission gas bubble growth on grain boundaries and triple junctions in UO2 nuclear fuel. Comput. Mater. Sci. **161**, 35 (2019)
J.B. Ainscough, B.W. Oldfield, J.O. Ware, Isothermal grain growth kinetics in sintered UO2 pellets. J. Nucl. Mater. **49**, 117 (1973)
C. Baker, The fission gas bubble distribution in uranium dioxide from high temperature irradiated Sghwr fuel pins. J. Nucl. Mater. **66**, 283 (1977)
S. Balay, S. Abhyankar, M. F. Adams, J. Brown, P. Brune, K. Buschelman, L. Dalcin, V. Eijkhout, W. D. Gropp, D. Kaushik, M. G. Knepley, D. A. May, L. C. McInnes, R. T. Mills, T. Munson, K. Rupp, P. Sanan, B. F. Smith, S. Zampini, H. Zhang, and H. Zhang, PETSc Users Manual, No. ANL-95/11-Revision 3.13, Argonne National Laboratory, 2020
S. Blondel, D.E. Bernholdt, K.D. Hammond, L. Hu, D. Maroudas, B.D. Wirth, Benchmarks and tests of a multidimensional cluster dynamics model of helium implantation in tungsten. Fusion Sci. Technol. **71**, 84 (2017)
S. Blondel, D.E. Bernholdt, K.D. Hammond, B.D. Wirth, Continuum-scale modeling of helium bubble bursting under plasma-exposed tungsten surfaces. Nucl. Fusion **58**, 126034 (2018)
A. Booth, A method of calculating gas diffusion from UO2 fuel and its application to the X-2-f test, technical report technical report AECL 496 CRDC-721. Atomic Energy of Canada Limited (1957)
P. Chakraborty, Y. Zhang, M.R. Tonks, Multi-scale modeling of microstructure dependent Intergranular brittle fracture using a quantitative phase-field based method. Comput. Mater. Sci. **113**, 38 (2016)
L.-Q. Chen, Phase-field models for microstructure evolution. Annu. Rev. Mater. Res. **32**, 113 (2002)
M.W.D. Cooper, G. Pastore, Y. Che, C. Matthews, A. Forslund, C.R. Stanek, K. Shirvan, T. Tverberg, K.A. Gamble, B. Mays, D.A. Andersson, Fission gas diffusion and release for Cr2O3-doped UO2: From the atomic to the engineering scale. J. Nucl. Mater. **152590** (2020)
R.M. Cornell, M.V. Speight, B.C. Masters, The role of bubbles in fission gas release from uranium dioxide. J. Nucl. Mater. **30**, 170 (1969)
A. Dunn, L. Capolungo, Simulating radiation damage accumulation in α-Fe: A spatially resolved stochastic cluster dynamics approach. Comput. Mater. Sci. **102**, 314 (2015)
A. Dunn, R. Dingreville, E. Martínez, L. Capolungo, Synchronous parallel spatially resolved stochastic cluster dynamics. Comput. Mater. Sci. **120**, 43 (2016)
A.Y. Dunn, L. Capolungo, E. Martinez, M. Cherkaoui, Spatially resolved stochastic cluster dynamics for radiation damage evolution in nanostructured metals. J. Nucl. Mater. **443**, 128 (2013)
K. Forsberg, A.R. Massih, Fission gas release under time-varying conditions. J. Nucl. Mater. **127**, 141 (1985)
D. Gaston, C. Newman, G. Hansen, D. Lebrun-Grandié, MOOSE: A parallel computational framework for coupled Systems of Nonlinear Equations. Nucl. Eng. Des. **239**, 1768 (2009)
D.R. Gaston, C.J. Permann, J.W. Peterson, A.E. Slaughter, D. Andrš, Y. Wang, M.P. Short, D.M. Perez, M.R. Tonks, J. Ortensi, L. Zou, R.C. Martineau, Physics-based multiscale coupling for full Core nuclear reactor simulation. Ann. Nucl. Energy **84**, 45 (2015)
S. Hu, D. Burkes, C.A. Lavender, V. Joshi, Effect of grain morphology on gas bubble swelling in UMo fuels – A 3D microstructure dependent Booth model. J. Nucl. Mater. **480**, 323 (2016)
S. Hu, C.H. Henager Jr., H.L. Heinisch, M. Stan, M.I. Baskes, S.M. Valone, Phase-field modeling of gas bubbles and thermal conductivity evolution in nuclear fuels. J. Nucl. Mater. **392**, 292 (2009)
S. Hu, V. Joshi, C.A. Lavender, A rate-theory–phase-field model of irradiation-induced recrystallization in UMo nuclear fuels. JOM **69**, 2554 (2017)
S. Hu, W. Setyawan, B.W. Beeler, J. Gan, D.E. Burkes, Defect cluster and nonequilibrium gas bubble associated growth in irradiated UMo fuels – A cluster dynamics and phase field model. J. Nucl. Mater. **542**, 152441 (2020)
W. Jiang, T. Hu, L.K. Aagesen, Y. Zhang, Three-dimensional phase-field modeling of porosity dependent Intergranular fracture in UO2. Comput. Mater. Sci. **171**, 109269 (2020)
S. Kashibe, K. Une, K. Nogita, Formation and growth of Intragranular fission gas bubbles in UO2 fuels with Burnup of 6–83 GWd/t. J. Nucl. Mater. **206**, 22 (1993)
Y. Li, S. Hu, R. Montgomery, F. Gao, X. Sun, Phase-field simulations of Intragranular fission gas bubble evolution in UO2 under post-irradiation thermal annealing. Nucl. Instrum. Methods Phys. Res. Sect. B Beam Interact. Mater. At. **303**, 62 (2013)
Y. Li, S. Hu, X. Sun, M. Stan, A. Review, Applications of the phase field method in predicting microstructure and property evolution of irradiated nuclear materials. Npj Comput. Mater. **3**, 1 (2017)
X.-Y. Liu, D.A. Andersson, Molecular dynamics study of fission gas bubble nucleation in UO2. J. Nucl. Mater. **462**, 8 (2015)
P. Lösönen, On the behaviour of Intragranular fission gas in UO2 fuel. J. Nucl. Mater. **280**, 56 (2000)
D. Maroudas, S. Blondel, L. Hu, K.D. Hammond, B.D. Wirth, Helium segregation on surfaces of plasma-exposed tungsten. J. Phys. Condens. Matter **28**, 064004 (2016)
A.R. Massih, K. Forsberg, Calculation of grain boundary gaseous swelling in UO2. J. Nucl. Mater. **377**, 406 (2008)
C. Matthews, R. Perriot, M.W.D. Cooper, C.R. Stanek, D.A. Andersson, Cluster dynamics simulation of uranium self-diffusion during irradiation in UO2. J. Nucl. Mater. **527**, 151787 (2019)
C. Matthews, R. Perriot, M.W.D. Cooper, C.R. Stanek, D.A. Andersson, Cluster dynamics simulation of xenon diffusion during irradiation in UO2. J. Nucl. Mater. **540**, 152326 (2020)

P.C. Millett, A. El-Azab, D. Wolf, Phase-field simulation of irradiated metals: Part II: Gas bubble kinetics. Comput. Mater. Sci. **50**, 960 (2011)
P.C. Millett, M. Tonks, Application of phase-field modeling to irradiation effects in materials. Curr. Opin. Solid State Mater. Sci. **15**, 125 (2011)
P.C. Millett, M.R. Tonks, S.B. Biner, L. Zhang, K. Chockalingam, Y. Zhang, Phase-field simulation of Intergranular bubble growth and percolation in Bicrystals. J. Nucl. Mater. **425**, 130 (2012)
N. Moelans, B. Blanpain, P. Wollants, An introduction to phase-field modeling of microstructure evolution. Calphad **32**, 268 (2008)
P.V. Nerikar, K. Rudman, T.G. Desai, D. Byler, C. Unal, K.J. McClellan, S.R. Phillpot, S.B. Sinnott, P. Peralta, B.P. Uberuaga, C.R. Stanek, Grain boundaries in uranium dioxide: Scanning Electron microscopy experiments and atomistic simulations. J. Am. Ceram. Soc. **94**, 1893 (2011)
M. OGUMA, Microstructure effects on fracture strength of U02 fuel pellets. J. Nucl. Sci. Technol. **19**, 1005 (1982)
D. R. Olander, Fundamental Aspects of Nuclear Reactor Fuel Elements, No. TID-26711-P1, California Univ., Berkeley (USA). Dept. of Nuclear Engineering, 1976
G. Pastore, L. Luzzi, V. Di Marcello, P. Van Uffelen, Physics-based Modelling of fission gas swelling and release in UO2 applied to integral fuel rod analysis. Nucl. Eng. Des. **256**, 75 (2013)
G. Pastore, D. Pizzocri, C. Rabiti, T. Barani, P. Van Uffelen, L. Luzzi, An effective numerical algorithm for intra-granular fission gas release during non-equilibrium trapping and resolution. J. Nucl. Mater. **509**, 687 (2018)
C.J. Permann, D.R. Gaston, D. Andrš, R.W. Carlsen, F. Kong, A.D. Lindsay, J.M. Miller, J.W. Peterson, A.E. Slaughter, R.H. Stogner, R.C. Martineau, MOOSE: Enabling massively parallel multiphysics simulation. SoftwareX **11**, 100430 (2020)
C.J. Permann, M.R. Tonks, B. Fromm, D.R. Gaston, Order parameter re-mapping algorithm for 3D phase field model of grain growth using FEM. Comput. Mater. Sci. **115**, 18 (2016)
D. Pizzocri, G. Pastore, T. Barani, A. Magni, L. Luzzi, P. Van Uffelen, S.A. Pitts, A. Alfonsi, J.D. Hales, A model describing intra-granular fission gas behaviour in oxide fuel for advanced engineering tools. J. Nucl. Mater. **502**, 323 (2018)
A.A. Prudil, K.D. Colins, E.S. Thomas, M.J. Welland, Intra- and Intergranular fission gas transport on large irregular hexagonal grain networks by an included phase model. J. Nucl. Mater. **542**, 152456 (2020)
A.A. Prudil, E.S. Thomas, M.J. Welland, Network percolation using a two-species included phase model to predict fission gas accommodation and venting. J. Nucl. Mater. **515**, 170 (2019)
J. Rest, M.W.D. Cooper, J. Spino, J.A. Turnbull, P. Van Uffelen, C.T. Walker, Fission gas release from UO2 nuclear fuel: A Review. J. Nucl. Mater. **513**, 310 (2019)
D. Schwen, L.K. Aagesen, J.W. Peterson, M.R. Tonks, Rapid multiphase-field model development using a modular free energy based approach with automatic differentiation in MOOSE/MARMOT. Comput. Mater. Sci. **132**, 36 (2017)
W. Setyawan, M.W.D. Cooper, K.J. Roche, R.J. Kurtz, B.P. Uberuaga, D.A. Andersson, B.D. Wirth, Atomistic model of xenon gas bubble re-solution rate due to thermal spike in uranium oxide. J. Appl. Phys. **124**, 075107 (2018)
R. Skorek, S. Maillard, A. Michel, G. Carlot, E. Gilabert, T. Jourdan, Modelling fission gas bubble distribution in UO_2. Defect Diffus. Forum **323–325**, 209 (2012)
M.V. Speight, A calculation on the migration of fission gas in Material Exhibiting Precipitation and re-Solution of gas atoms under irradiation. Nucl. Sci. Eng. **37**, 180 (1969)
M. Tonks, D. Andersson, R. Devanathan, R. Dubourg, A. El-Azab, M. Freyss, F. Iglesias, K. Kulacsy, G. Pastore, S.R. Phillpot, M. Welland, Unit mechanisms of fission gas release: Current understanding and future needs. J. Nucl. Mater. **504**, 300 (2018a)
M.R. Tonks, L.K. Aagesen, The phase field method: Mesoscale simulation aiding material discovery. Annu. Rev. Mater. Res. **49**, 79 (2019)
M.R. Tonks, A. Cheniour, L. Aagesen, How to apply the phase field method to model radiation damage. Comput. Mater. Sci. **147**, 353 (2018b)
M.R. Tonks, D. Gaston, P.C. Millett, D. Andrs, P. Talbot, An object-oriented finite element framework for multiphysics phase field simulations. Comput. Mater. Sci. **51**, 20 (2012)
M.R. Tonks, X.-Y. Liu, D. Andersson, D. Perez, A. Chernatynskiy, G. Pastore, C.R. Stanek, R. Williamson, Development of a multiscale thermal conductivity model for fission gas in UO2. J. Nucl. Mater. **469**, 89 (2016)
M.R. Tonks, P.-C.A. Simon, J. Hirschhorn, Mechanistic grain growth model for fresh and irradiated UO2 nuclear fuel. J. Nucl. Mater. **543**, 152576 (2021)
J.A. Turnbull, The effect of grain size on the swelling and gas release properties of Uo2 during irradiation. J. Nucl. Mater. **50**, 62 (1974)
J.A. Turnbull, C.A. Friskney, J.R. Findlay, F.A. Johnson, A.J. Walter, The diffusion coefficients of gaseous and volatile species during the irradiation of uranium dioxide. J. Nucl. Mater. **107**, 168 (1982)
R. White, R. Corcoran, P. Barnes, A summary of swelling data obtained from the AGR/Halden ramp test Programme. Tech Rep RTNGEXTREP020602 (2006)
R.J. White, The development of grain-face porosity in irradiated oxide fuel. J. Nucl. Mater. **325**, 61 (2004)
R.J. White, M.O. Tucker, A new fission-gas release model. J. Nucl. Mater. **118**, 1 (1983)
B.D. Wirth, X. Hu, A. Kohnert, D. Xu, Modeling defect cluster evolution in irradiated structural materials: Focus on comparing to high-resolution experimental characterization studies. J. Mater. Res. **30**, 1440 (2015)
D. Xu, B.D. Wirth, Modeling spatially dependent kinetics of helium desorption in BCC Iron following he ion implantation. J. Nucl. Mater. **403**, 184 (2010)
Y. Zhu, H. Hallberg, Investigation of faceted void morphologies in UO2 by phase field Modelling. J. Nucl. Mater. **467**, 113 (2015)

Publisher's Note